Journal of Catalysis 277 (2011) 196–207

Contents lists available at ScienceDirect

Journal of Catalysis

journal homepage: www.elsevier.com/locate/jcat

Impact of phosphorus and nitrogen on structure and catalytic performance of VZrPON oxynitrides in the ammoxidation of 3-picoline

C. Janke [a], M. Schneider [a], U. Bentrup [a], J. Radnik [a], A. Martin [a], G. Scholz [b], A. Brückner [a,*]

[a] Leibniz-Institut für Katalyse e. V. an der Universität Rostock, Albert-Einstein-Str 29a, D-18059 Rostock, Germany
[b] Humboldt-Universität zu Berlin, Institut für Chemie, Brook-Taylor-Str. 2, D-12489 Berlin, Germany

ARTICLE INFO

Article history:
Received 3 September 2010
Revised 9 November 2010
Accepted 11 November 2010

Keywords:
Vanadium zirconium phosphorus oxynitrides
In situ-EPR/UV–vis/Raman spectroscopy
Ammoxidation
3-Picoline

ABSTRACT

Novel P-containing oxynitrides VZrPON were tested besides their VZrPO oxide precursors in the ammoxidation of 3-picoline and compared with P-free VZrON catalysts for analysing the influence of both incorporated P and N on the catalytic performance. Results of XRD, XPS, ^{31}P and ^{51}V MAS NMR as well as of simultaneous in situ-EPR/UV–vis/Raman studies during nitridation have shown that the incorporation of phosphorus enhances the V dispersion, reduces vanadium partially even down to V^{3+} and leads to the formation of a crystalline $ZrV_{2-x}P_xO_7$ phase for $Zr/V \geqslant 0.5$ with V sites surrounded by four O atoms only. N is preferentially incorporated in the vicinity of P, thus, suppressing the formation of V—N moieties. These facts may be a reason why the incorporation of P does not markedly improve the catalytic performance of VZrPON catalysts.

1. Introduction and objective

Ammoxidation of 3-picoline (3-PIC) in the gas phase is an important industrial process to produce nicotinonitrile (or 3-cyanopyridine, 3-CP), which is the starting material for the production of nicotinic acid and nicotinic amide [1–3]. The latter two compounds are essential vitamins and widely applied in the agrochemical and pharmaceutical sector [4]. Most prominent catalysts for this reaction are mixed oxides based on V/Ti, V/Mo, V/Sn or V/Sb compositions, which all contain vanadium as redox-active component [5–7]. One of the industrial benchmark catalysts is a SbVTiSi-KO mixed oxide by which 3-CP selectivities as high as 92–96% are reached at 3-PIC conversions of 89–97% and space–time yields (STY) of 146–156 $g l^{-1} h^{-1}$ [8]. Also, supported vanadium oxide and VPO catalysts have been tested in the ammoxidation of 3-PIC [9–12].

Recently, we have reported on novel VAlON and VZrON oxynitride catalysts which showed even higher space–time yields in the ammoxidation of 3-PIC [13]. Thus, with VZrON systems, we obtained three times higher STY values of 3-CP than those of the benchmark system, yet with somewhat lower selectivities. Improving the selectivity of such materials while maintaining the high space–time yields would be a worthwhile goal for further research which calls for a dedicated introduction of structural moieties that favour high selectivities. However, this requires detailed knowledge on the reaction mechanism and structural key features which govern the selectivity of oxynitrides.

Within the last three decades, comprehensive mechanistic investigations have been performed in the ammoxidation of alkylaromatics and heteroaromatics over oxide catalysts, starting with the early work of Andersson et al. [14], while no such studies are available for oxynitrides. Some years ago, a review has been published which highlights the main aspects of the role of oxide catalysts [15]. Active sites are considered to be an ensemble of neighbouring vanadyl species [16]. Based on the excellent catalytic results obtained over $(VO)_2P_2O_7$, it was proposed that those sites should contain surface vanadyl species with a proper distance to enable simultaneous adsorption of the aromatic π-system and conversion of the methyl group in neighbouring positions [17]. Moreover, chain- or layer-like vanadyl structures are assumed to be beneficial, since the electronic coupling between them should support the electron transport from surface to bulk and vice versa [18].

For oxide catalysts, it has been proposed that the reaction starts with adsorption of the aromatic ring followed by hydrogen abstraction from the alkyl group, formation of a benzyl-like intermediate and in situ generation of an —OH group that converts gaseous NH_3 to NH_4^+ by proton transfer. In due course, the NH_4^+ ions are supposed to react with the benzyl species to a benzylamine intermediate, which is transformed to nitrile. A Mars–van Krevelen mechanism including participation of lattice oxygen proceeded during this reaction [19,20]. Also, imido =NH or amido —NH_2 species on the catalyst surface are considered as active N-insertion

* Corresponding author. Fax: +49 (0)381 1281 51244.
E-mail address: angelika.brueckner@catalysis.de (A. Brückner).

0021-9517/$ - see front matter © 2010 Elsevier Inc. All rights reserved.
doi:10.1016/j.jcat.2010.11.008

sites [21–23], but their role in the ammoxidation of aromatics is still not fully elucidated. The activation of NH_3 from the gas feed via transient incorporation into the catalyst lattice has been evidenced by isotopic labelling experiments using the Temporal-Analysis-of-Products (TAP) reactor and $^{15}NH_3$ as feed component [24]. It represents a crucial step within the reaction network insofar as oxide catalysts are not active when they are not able to activate ammonia in this way [21]. For VAlON oxynitride catalysts, which have been used for the ammoxidation of propane to acrylnitrile [25], TAP experiments with labelled $^{15}NH_3$ have shown, too, that N insertion into the hydrocarbon occurs via a surface N site [26,27]. Thus, the insertion of N and O via a double Mars–van Krevelen mechanism is considered to be responsible for their high catalytic performance in the ammoxidation of both propane [26,27] and 3-PIC [13].

For VZrON oxynitrides, even higher space–time yields as for VAlON catalysts were found in the ammoxidation of 3-PIC, however, at lower 3-CP selectivities. This has been attributed to the higher mean oxidation state and polymerization degree of the surface V sites as well as to the fact that almost the total N content is located in the bulk of the catalysts and, thus, hardly accessible to reactants [13]. If it was possible to stabilize active nitrogen sites on the catalyst surface, this could help to improve the selectivity of such materials. Within the class of oxides, $(VO)_2P_2O_7$ belongs to the best catalysts for the ammoxidation of methylaromatics [15]. For this material, it has been shown that the incorporation of active N sites in the surface is promoted by ammonolysis of the P—O—V bonds giving rise to NH_4^+ and NH_2^- surface groups. This suggests that phosphorus plays a beneficial role for the N enrichment of the $(VO)_2P_2O_7$ surface under ammoxidation conditions. On the other hand, zirconium phosphate oxynitrides (ZrPON) are known to possess a N-rich surface. Different N sites such as nitride N^{3-} and NH_x ($1 \leqslant x \leqslant 4$) have been detected in these materials depending on the nitridation conditions of the oxide precursors [28]. However, these materials might not catalyse ammoxidation reactions since the essential redox-active vanadium component is missing.

Therefore, we have synthesized new VZrPON catalysts by incorporating phosphorus into the VZrO precursor, followed by nitridation. The aim was to promote, with the help of phosphorus, the stabilization of N sites in the surface of VZrPON catalysts and to explore the influence of structural properties created by these elements on activity and selectivity in the ammoxidation of 3-PIC to 3-CP. A comprehensive approach comprising catalytic tests and spectroscopic investigations was followed to derive structure–reactivity relationships, including simultaneous in situ-EPR/UV–vis/Raman studies.

2. Experimental

2.1. Catalyst synthesis

VZrPO oxide precursors were synthesized by the citrate method with V/Zr ratios of 0.1, 0.5 and 0.9. Respective samples are denoted as VZrPO-*x.x*, with *x.x* being the V/Zr ratio. The atomic Zr/P ratio was adjusted to 0.9 (V + Zr ≠ const.). The desired amount of NH_4VO_3 (Sigma–Aldrich, 99%) was suspended in water under stirring at 70 °C (0.02 M) and subsequently acidified with HNO_3 (19 M) to pH = 3. A second solution was prepared by dissolving the appropriate amount of $ZrO(NO_3)_2$ (Sigma–Aldrich, tech.) in water under stirring at 70 °C (0.02 M). To this solution, the acidic NH_4VO_3 solution was added under stirring at 70 °C. After adding the corresponding amount of phosphoric acid (3 M), a gel was formed, which was stirred for 1 h at 70 °C, before 55 g of solid citric acid was added under stirring. Different blue colours were observed depending on V concentration in solution. These solutions were refluxed for 16 h under stirring at 70 °C. Water was evaporated using a rotating evaporator, and the resulting brown powder was dried at 120 °C for 16 h. After grinding, the powder was calcined in air (6 l/h) for 16 h at 500 °C and for another 6 h at 600 °C to remove carbon. The resulting yellow powders were carbon free.

The VZrPO precursors were pressed and crushed to particles with a diameter between 0.8 and 1 mm. In a home-made shaking fluidized bed reactor, 6 ml of VZrPO particles were loaded. Precursors were treated in flowing NH_3 (40 l/h) for 6 h at 500 °C. During this treatment, the sample colour turned from yellow to grey or black depending on the V concentration. The resulting oxynitrides are denoted as VZrPON-*x.x* with *x.x* being the V/Zr ratio.

2.2. Catalytic tests

Catalytic tests were performed in a fixed bed glass reactor (inner diameter = 1.5 cm) with 3 ml of catalyst particles of 1.0–1.25 mm diameter, diluted in a ratio of 1:1 with glass particles of the same size [9]. A gas feed flow with a molar ratio of 3-PIC:air:NH_3:H_2O = 1:22:4:8 was passed over the catalyst with a gas hourly space velocity (GHSV) of 3242 h^{-1} for VZrPO and VZrPON samples and 5728 h^{-1} for VZrON catalysts. The liquid feed components were fed into the gas stream by continuous evaporation of a 1.5:1 (vol.%) 3-PIC (Aldrich, 99%)/water mixture using a syringe pump (Cole-Parmer Instrument Company). Gaseous feed components were dosed by mass flow controllers (Bronkhorst). The catalyst bed temperature inside the reactor was adjusted to 360 °C for all catalytic experiments and measured during reaction using a thermocouple inside of the reactor. The products were collected in a cold trap and analysed offline using a GC-17A (Shimadzu) equipped with an auto sampler (AOC-20i) and a WCOT fused Silica CP-SIL 8CB column (Varian). Carbon oxides were determined online by a non-dispersive infrared analyser (BINOS100 2M, Rosemount). Carbon balances calculated from experimental data were always higher than 98%. To distinguish between fresh and used catalysts, the latter are denoted with the letter A at the end of the sample name.

The effect of time on stream on the catalytic performance was investigated with 3 ml of the fresh catalyst VZrPON-0.53. The molar ratio of the gas feed flow, catalyst bed temperature and GHSV were adjusted as described previously. Analyses of the products were taken every 20 min.

To elucidate the influence of the feed composition on the catalytic performance at a catalyst bed temperature of 360 °C, the respective flows of ammonia $F(NH_3)$ and air $F(\text{air})$ were modified. The ratio $F(NH_3)/F(\text{air})$ was varied between 2.6 and 9.2. The total flow of the feed stream was balanced with N_2 to maintain a GHSV of 3242 h^{-1}.

2.3. Catalyst characterization

XRD powder patterns were recorded in transmission geometry with Cu $K\alpha_1$ radiation on a Stoe STADI P diffractometer, equipped with a position sensitive detector (PSD). Processing and assignment of the powder patterns was done using the software Win Xpow (Stoe) and the powder diffraction file (PDF) database of the International Centre of Diffraction Data (ICDD).

ICP-OES measurements were performed with a Varian 715-ES spectrometer calibrated for the required elements. All values were verified by double determination. Ten milligrams of catalyst was dissolved in 4 ml HF and 4 ml aqua regia in a microwave oven (Anton Paar/Perkin-Elmer) at ca. 60 bar and ca. 120 °C. The obtained solution was filled up to 100 ml with distilled water and measured.

CHN analysis was performed with an EA 1110 CHN analyser (CE Instrumenta) calibrated for the required elements and equipped with an autosampler. In a home-made tin crucible, 10–30 mg of each catalyst powder was placed. Measured data were evaluated with Eager 200 for windows software. All values were verified by double determination.

^{31}P and ^{51}V MAS NMR spectra were recorded on a Bruker AVANCE 400 spectrometer (Larmor frequencies: ν_{31P} = 161.9 MHz; ν_{51V} = 105.2 MHz) using a 2.5 mm magic angle spinning (MAS) probe (Bruker Biospin). ^{51}V MAS NMR (I = 7/2) spectra were recorded with a sweep width of 1 MHz and an excitation pulse duration of 0.8 μs ensuring a linear irradiation regime for reducing the distortion of the spectra. $VOCl_3$ was used as reference for the chemical shift of ^{51}V. The recycle delay was chosen as 1 s, and accumulation numbers of 10,060 (sample VZrPO-0.9, ν_{rot} = 28 kHz) and 62,800 (sample VZrPON-0.9, ν_{rot} = 25 kHz), respectively, were used for an acceptable signal-to-noise ratio. ^{31}P MAS NMR measurements (ν_{rot} = 25 kHz) were performed with a recycle delay of 120 s, a $\pi/2$ pulse length of 6 μs and 180 (sample VZrPO-0.9) or 623 (sample VZrPON-0.9) transients. ^{31}P chemical shifts are referenced against H_3PO_4.

FTIR spectra at ambient conditions were recorded in attenuated total reflection (ATR) mode using an Alpha-P FTIR spectrometer (Bruker). Selected spectra were recorded at room temperature in transmission mode on a Nicolet 6700 FTIR spectrometer equipped with a heatable and evacuable IR cell and CaF_2 windows. In this case, 50 mg of each catalyst powder was pressed to a self-supporting wafer and heated to 300 °C under vacuum before collecting the spectrum. Surface acidity was analysed by transmission FTIR spectroscopy (Bruker IFS 66) of pyridine adsorbed at 20 °C on self-supporting wafers after pretreatment in flowing air at 300 °C, using the band areas at 1540 cm^{-1} for Brønsted sites.

X-ray photoelectron spectra (XPS) were recorded on a VG ESCALAB 220iXL instrument with Mg Kα radiation (E = 1253.6 eV). The samples were fixed with a double-adhesive carbon tape on a stainless steel sample holder. The peaks were fitted by Gaussian–Lorentzian curves after Shirley background subtraction. The electron binding energy was referenced to the carbon 1s peak at 284.8 eV. For quantitative analysis of the near-surface region, the peak areas were determined and divided by the element-specific Scofield factor and the analysator-depending transmission function.

Simultaneous in situ-EPR/UV–vis/Raman studies during treatment in N_2 and NH_3/N_2 flow were performed using the equipment described previously in detail [29]. Then, 115 mg catalyst particles (315–710 μm) were heated in N_2 flow (10 ml/min) to 120 °C, before switching to 20% NH_3/N_2 (50 ml/min) at the same temperature.

EPR spectra in X-band ($\nu \approx 9.5$ GHz) were recorded on an EPR cw-spectrometer ELEXSYS 500-10/12 (Bruker) at a microwave power of 6.3 mW, a modulation frequency of 100 kHz and a modulation amplitude of 0.5 mT. The magnetic field was measured with respect to the standard 2,2-diphenyl-1-picrylhydrazyl hydrate (DPPH). Computer simulation of EPR spectra was performed with the program SIM14S of Lozos et al. [30] using the spin Hamiltonian

$$H = \mu_B \cdot S \cdot g \cdot B_0 + SAI \quad (1)$$

in which μ_B is the Bohr magneton, S is the electron spin operator, g is the g tensor, B_0 is the magnetic field vector, A is the hyperfine tensor, and I is the nuclear spin operator.

Raman spectra were measured with a laser power of 50 mW and an acquisition time of 4–8 s. For each spectrum, 4–8 scans were accumulated. The beam of a 785 nm diode laser of a Kaiser Optical Systems RXN spectrometer was focused through a front hole in the EPR cavity onto the catalyst bed within the reactor.

UV–vis spectra were simultaneously collected in reflectance mode and converted into Kubelka–Munk (KM) functions by an AVASPEC fibre optical spectrometer (Avantes) using a quartz sensor (Optran UV 1500/1800 T, CeramOptec GmbH), which was directly inserted into the catalyst bed through the top of the EPR flow reactor [30].

The BET surface area of each catalyst was determined by nitrogen adsorption at 77 K (ASAP2010).

3. Results and discussion

3.1. Catalytic properties of VZrPO precursors and VZrPON oxynitrides

In Fig. 1, the conversions of 3-PIC ($X_{3\text{-PIC}}$) and selectivities towards 3-CP ($S_{3\text{-CP}}$) at 360 °C are plotted as a function of the V/Zr ratio for the VZrPON oxynitride catalysts and the VZrPO oxide precursors, which have not been pretreated in NH_3 flow. For comparison, the results of the P-free VZrON catalysts (taken from Ref. [13]) are also shown. Interestingly, although the BET surface areas of the VZrPON samples are somewhat lower (Table 1), VZrPO and VZrPON samples with equal V content show identical conversion values, which pass through a maximum at a medium ratio of V/Zr = 0.56. The 3-CP selectivity over the N-free VZrPO precursor is slightly higher than for the VZrPON catalysts at lower V content but falls below the selectivity of the latter at the highest V/Zr ratio. In comparison with the P-containing VZrPON oxynitrides, the previously studied P-free VZrON catalysts are much more active at low V/Zr ratios, while the 3-CP selectivity is comparable to that of the VZrPON catalysts. (dashed lines in Fig. 1). Thus, it turns out that the introduction of P into the VZrON structure does not lead to the desired improvement of the catalytic performance. This is surprising since, based on literature data over VPO catalysts, a positive effect on the catalytic performance was expected. To find reasons for this unexpected behaviour, a detailed characterization study is presented below to discover the role of phosphorus with respect to structure and catalytic performance of VZrPON oxynitrides.

In Fig. 2A, the catalytic performance of the oxynitride VZrPON-0.53 is shown depending on reaction time. While $X_{3\text{-PIC}}$ is nearly constant, $S_{3\text{-CP}}$ is slightly changing with time on stream. Starting from 65%, selectivity drops after 40 min to a minimum of 59% and returns afterwards to ca. 62%. Apparently, the structure of the oxynitride catalyst is changing during the initial reaction period.

In Fig. 2B, the catalytic performance of VZrPON-0.53 is depicted as a function of the air and ammonia feed ratio $F(\text{air})/F(NH_3)$. It can

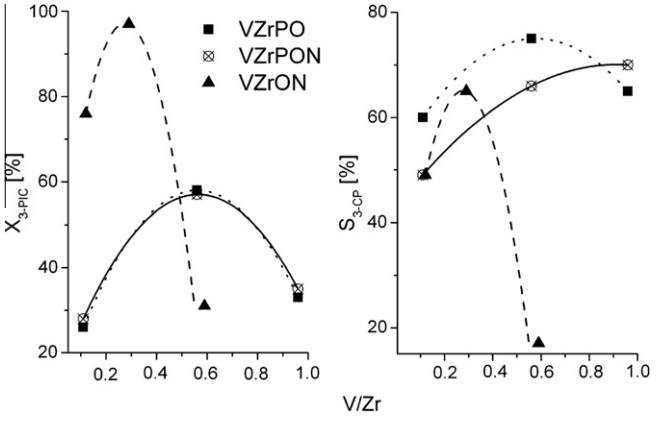

Fig. 1. Conversion of 3-picoline ($X_{3\text{-PIC}}$) and selectivity of 3-cyanopyridine ($S_{3\text{-CP}}$) measured at 360 °C for VZrPO oxide precursors and VZrPON oxynitrides. For comparison, values of P-free VZrON (taken from Ref. [9]) are also shown.

Table 1
Surface area (S_{BET}), bulk and surface composition of fresh and used oxide precursors and nitrided catalysts.

Catalyst	S_{BET} ($m^2 g^{-1}$)	Composition, fresh[a]	Fresh[b]					Used[b]				
			wt.% N[a]	Zr/V	Zr/P	N/V	N/P	wt.% N[a]	Zr/V	Zr/P	N/V	N/P
VZrPO-0.1	192	$ZrV_{0.11}P_{1.18}O_{6.23}$	0	9.10	0.84	–	–	2.67	–	–	–	–
				(5.88)	(0.76)	–	–		(2.26)	(0.81)	(1.20)	(0.36)
VZrPO-0.5	75	$ZrV_{0.56}P_{1.22}O_{7.86}$	0	1.78	0.82	–	–	1.86	–	–	–	–
				(2.00)	(0.64)	–	–		–	–	–	–
VZrPO-0.9	52	$ZrV_{0.96}P_{1.19}O_{7.59}$	0	1.04	0.84	–	–	0.51	–	–	–	–
				(0.86)	(0.62)	–	–		–	–	–	–
VZrPON-0.1	122	$ZrV_{0.11}P_{1.16}O_{6.71}N_{0.59}$	3.35	9.10	0.86	5.36	0.51	2.94	–	–	–	–
				(6.67)	(0.65)	(2.00)	(0.19)		(5.48)	(0.69)	(1.89)	(0.24)
VZrPON-0.5	65	$ZrV_{0.56}P_{1.21}O_{6.15}N_{0.53}$	2.83	1.78	0.83	0.95	0.44	2.60	–	–	–	–
				(1.74)	(0.63)	(0.71)	(0.26)		(1.65)	(0.67)	(0.78)	(0.32)
VZrPON-0.9	25	$ZrV_{0.97}P_{1.17}O_{7.40}N_{0.47}$	2.91	1.03	0.85	0.48	0.40	1.61	–	–	–	–
				(1.25)	(0.61)	(0.43)	(0.21)		(1.03)	(0.64)	(0.55)	(0.34)

[a] Derived by CHN analysis and ICP-OES.
[b] Values in brackets reflect surface values derived by XPS.

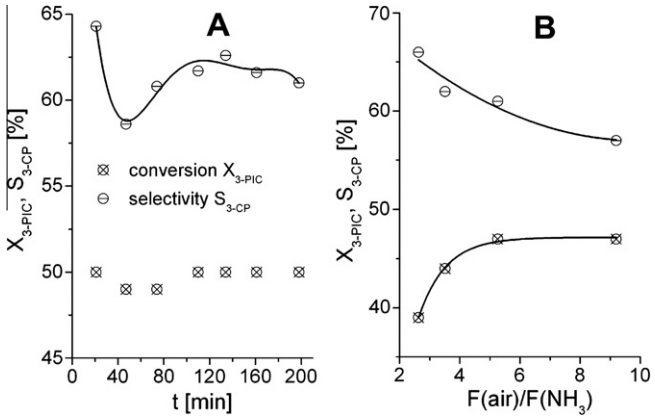

Fig. 2. Conversion of 3-picoline ($X_{3\text{-PIC}}$) and selectivity of 3-cyanopyridine ($S_{3\text{-CP}}$) measured at 360 °C for VZrPON-0.53 as a function of time on stream (A) and as a function of the flow ratio $F(air)/F(NH_3)$ at a reaction time of ca. 1 h for each ratio (B).

be seen that $X_{3\text{-PIC}}$ increases with rising air content in the feed up to a ratio of $F(air)/F(NH_3) = 5$ and then remains virtually constant, while $S_{3\text{-CP}}$ decreases continuously upon lowering the NH_3 content. This shows clearly that a high NH_3 concentration is essential to maintain high selectivity, while high activity is mainly related to a high oxygen concentration.

3.2. Structural properties of VZrPO precursors and VZrPON catalysts

3.2.1. XRD results

XRD patterns of the fresh VZrPO oxide precursors are shown in Fig. 3A. While sample VZrPO-0.1 is essentially amorphous, sample VZrPO-0.9 shows well-pronounced reflections indicating the presence of a crystalline phase which starts to form already at a ratio of V/Zr = 0.5. The intensity of these reflections increases after use in the ammoxidation of 3-PIC for V/Zr ratios higher than 0.5, while the used VZrPO-0.1 catalyst remains amorphous (Fig. 3C). In general, the same XRD peaks, though with much lower intensity, are observed for the VZrPON-0.9 oxynitride, while VZrPON catalysts with lower V content are completely amorphous (Fig. 3B). This suggests that nitridation of the oxide precursor destroys this crystalline phase. As for the oxide precursor, the XRD reflections of sample VZrPON-0.9 gain intensity after use in ammoxidation pointing to a slight increase in crystallinity; however, the crystalline phase remains much less pronounced than in the oxide precursor (compare Fig. 3C and D).

This crystalline phase is not part of the powder diffraction file database of the International Centre of Diffraction Data (ICDD), yet the positions of the reflections in Fig. 3 fall right between those of the isostructural binary cubic ZrV_2O_7 and ZrP_2O_7 phases [31,32] and the relative peak intensities are also very similar (Fig. S1). In cubic ZrM_2O_7 compounds (M = V or P), MO_4 tetrahedra are connected via M-O-M bridges to dimers, which surround the ZrO_6 octahedra. Due to the strong similarities of the XRD patterns in Fig. 3 with those of the binary compounds (Fig. S1), we supposed that the patterns in Fig. 3 may arise from a mixed $ZrVPO_7$ phase in which V and P occupy the centres of MO_4 tetrahedra statistically. The formation of such mixed phases in the ternary Zr—V—P oxide system has been previously concluded from solid-state NMR measurements [33,34] and it was found that mixed VPO_7^{4-} dimers are prevailing over the pure $V_2O_7^{4-}$ and $P_2O_7^{4-}$ dimers when the Zr/M ratio is close to unity [34], as it is the case in the VZrPO-0.9 and VZrPON-0.9 samples.

3.2.2. ^{31}P and ^{51}V MAS NMR results

Therefore, we studied the latter two samples by solid-state MAS NMR spectroscopy to prove the formation of VPO_7^{4-} dimers (Fig. 4). The ^{31}P MAS NMR spectrum of the VZrPO-0.9 oxide precursor contains two peaks which are assigned to P in V—O—P units (−28.9 ppm) and in P—O—P units (−41.7 ppm) [33,34]. The signal at −822 ppm in the ^{51}V MAS NMR spectrum can be assigned to V within V—O—P moieties [33,34], while the second narrow line at −612 ppm is characteristic for V_2O_5 [35]. The NMR spectra of the oxynitride catalyst show the same signals for the mixed $ZrVPO_7$ phase, yet the line for V_2O_5 is missing (Fig. 4). This suggests that V_2O_5 is more easily reduced than $ZrVPO_7$ during nitridation by ammonia. The broad background signal in the ^{31}P spectrum of VZrPON-0.9 along with the worse signal-to-noise ratio obtained with an even larger number of accumulations suggests in agreement with XRD data that the major part of this catalyst might be amorphous, i.e., the crystalline $ZrVPO_7$ phase is markedly destroyed.

3.2.3. Bulk and surface composition

The bulk and surface compositions of fresh and used catalysts are compared in Table 1. The Zr/P ratio in the fresh oxide precursors is close to 0.9 as desired and this does not change after nitridation to the corresponding oxynitrides. Thus, a loss of P *via* the formation of volatile phosphine during ammonia treatment can be excluded. The Zr/P ratio on the surface is slightly lower than in the bulk for all fresh VZrPO and VZrPON samples, indicating that phosphorus is slightly enriched on the surface. The concentration of vanadium is almost the same in the bulk and in the surface

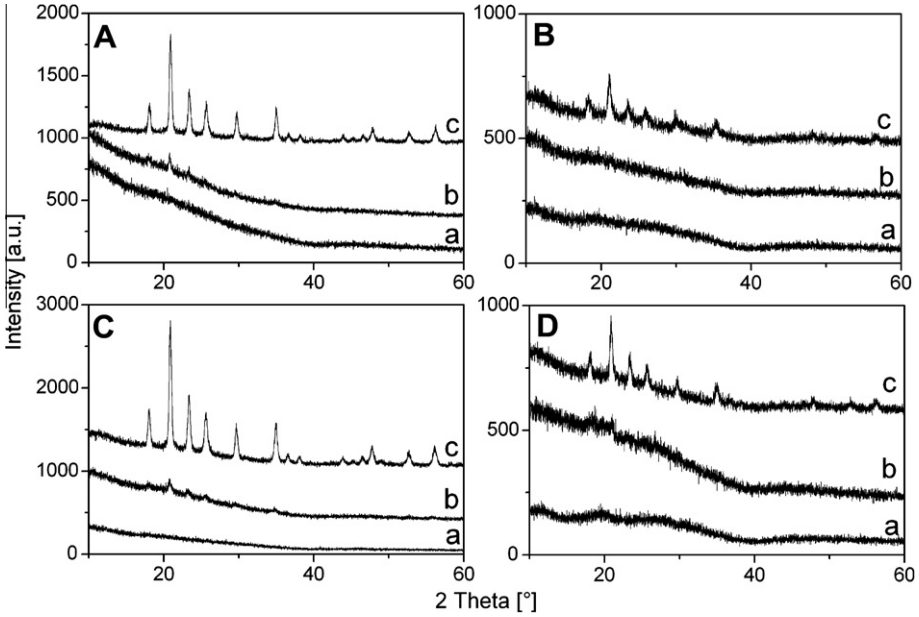

Fig. 3. Powder XRD patterns of fresh samples (A=VZrPO and B=VZrPON) and catalysts after use in 3-PIC ammoxidation (C=VZrPO and D=VZrPON) with different V/Zr ratios (a = 0.1, b = 0.5 and c = 0.9).

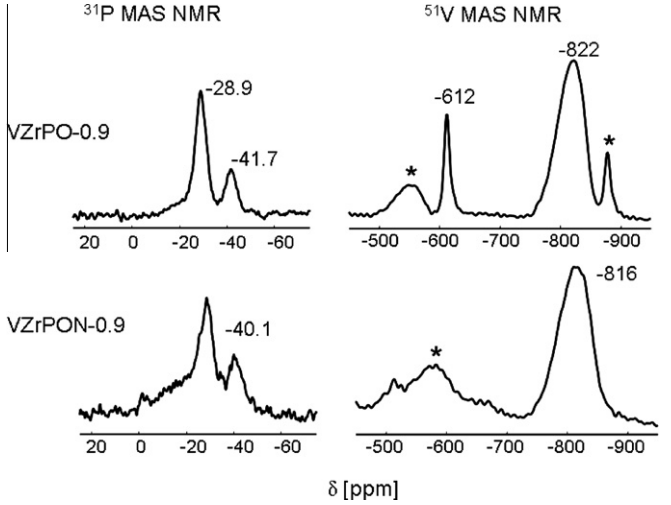

Fig. 4. ^{31}P (left) and ^{51}V (right) MAS NMR spectra for VZrPO-0.9 and VZrPON-0.9 measured at room temperature (*spinning side bands).

Table 2
Binding energies E_B and ΔE_B with $\Delta E_B = E_B(O1s) - E_B(V2p_{3/2})$ for fresh and used (denoted by A) VZrPON-x catalysts.

Catalyst	E_B (eV) O1s	E_B (eV) P2p	E_B (eV) V2p$_{3/2}$	E_B (eV) N1s	Percentage amount of N (%)	ΔE_{Bm} (eV)
VZrPO-0.1	530.4	132.6	516.7	–	–	13.7
VZrPO-0.5	530.4	132.6	516.8	–	–	13.6
VZrPO-0.9	530.3	132.7	516.8	–	–	13.5
VZrPO-0.1A	530.5	132.6	516.4	399.8	100	14.1
VZrPON-0.1	530.0	132.6	515.8	400.4	29.5	14.2
				398.2	70.5	
VZrPON-0.5	529.8	132.6	515.6	400.9	4.2	14.1
				398.4	95.8	
VZrPON-0.9	529.8	132.7	515.7	400.6	14.3	14.1
				398.6	85.7	
VZrPON-0.1A	530.4	132.6	516.8	400.7	51.3	13.6
				398.8	48.7	
VZrPON-0.5A	530.3	132.6	516.7	400.7	67.9	13.6
				399.0	32.1	
VZrPON-0.9A	530.3	132.6	516.7	401.0	45.5	13.6
				399.6	54.5	

except for VZrPO-0.1 and VZrPON-0.1. In these samples, vanadium is enriched in the surface, as reflected by the markedly lower Zr/V ratios.

The total N content and the N/V ratios in the VZrPON series decrease with rising V content, while the N/P ratios remain nearly constant. This suggests that P—O bonds may be more prone to nitridation than V—O bonds and incorporation of N in the oxide precursor is rather linked to the P content. In comparison with the bulk N/V ratios, the surface N/V ratios of the fresh VZrPON catalysts are lower, indicating that N is enriched to some extent in the bulk. Incorporation of nitrogen into the oxide precursors does not only occur during nitridation in NH_3 flow but also upon using the VZrPO precursors directly as catalysts in the ammoxidation of 3-PIC (Table 1, used samples). As likewise observed for fresh VZrPON catalysts, the total N content decreases for the used oxide precursors with rising V content. In contrast to the oxide precursors, the VZrPON oxynitrides loose nitrogen during use in the ammoxidation; however, the N percentage remaining in the structure is still higher than in the used VZrPO samples.

In the XPS spectra, the P2p peak is found at a binding energy of ca. 132.6 eV in all samples, which is very similar to the E_B values in VPO compounds [36]. However, differences were observed for the N1s and V2p$_{3/2}$ peaks (Table 2). From the difference of the binding energies of the O1s and the V2p$_{3/2}$ peak, $\Delta E_B = E_B(O1s) - E_B(V2p_{3/2})$, the mean V valence state can be estimated, based on ΔE_B values which have been derived for a series of vanadium oxides with known mean V valence [37]. This procedure is more reliable than using the binding energies of the V2p$_{3/2}$ peaks alone for deriving the mean V valence.

The ΔE_B values in Table 2 are essentially the same for all fresh oxynitrides and amount to 14.1 which corresponds to a mean V

valence of 4.0 according to the relation given in reference [37]. A slight decrease in ΔE_B values from 14.1 to 13.6 is observed for the whole catalyst series VZrPON after use in the ammoxidation reaction, which points to a slight increase in the surface V valence state from 4.0 to 4.3. ΔE_B values of fresh oxide precursors VZrPO-*x.x* are also similar, ranging between 13.5 and 13.7 eV which corresponds to a mean surface V valence of ≈4.3. From a comparison of the ΔE_B values of the fresh VZrPO-0.1 and used VZrPO-0.1A oxide precurors with those of the corresponding VZrPON-0.1 and VZrPON-0.1A oxynitrides, it can be concluded that the surface of the oxide precursors is slightly reduced during ammoxidation, while that of the oxynitrides is oxidized.

It must be mentioned that all XP spectra have been recorded from samples after contact with ambient atmosphere. This may have caused reoxidation of V^{3+}, which could have been formed after nitridation and/or ammoxidation. This aspect is discussed in more detail later with the in situ-EPR and -UV–vis studies.

Two different XPS peaks were detected in the N1s region for all fresh and used VZrPON catalysts in a range of 400.4–401.0 and 398.2–399.6 eV. Fripiat et al. [28] observed three different N1s peaks in ZrPON oxynitrides with Zr/P = 0.9. They assigned these peaks to nitride anions N^{3-} (397.7 eV), surface NH_x species with $1 \leqslant x \leqslant 4$ (399.2 eV) and NH_4^+ ions (400.4 eV). Based on this work, we attribute the peaks at 399.8–401.0 eV to NH_4^+ ions and the peaks at 398.2–399.6 eV to —NH_2 and/or —NH surface groups. Wiame et al. have studied the influence of nitridation temperature T_N on the nitrogen environment in VAlON catalysts using XPS [38]. They found surface species of the latter type already at a temperature of T_N = 250°, while nitride species in the vicinity of V began to form only at 500 °C and their amount increased with rising T_N.

In contrast to VAlON catalysts, the formation of nitridic V—N surface species can be excluded, since no peaks at typical binding energies like in VAlON catalysts (513.9 eV for V2$p_{3/2}$ and 395.9 eV for N1s [13]) are detected. Thus, it is likely that the second N surface site is rather connected to P or Zr which, however, does not change the position of the P2p peak. This may be due to the rather low amount of surface N species. The N/P surface ratio amounts to 0.19–0.34 only (Table 1). This means that nominally only one of the four P—O bonds is replaced by P—N. Most probably this is not enough to cause a P binding energy shift that differs significantly from experimental error, which is 0.1–0.2 eV.

Inspection of Table 2 shows that the binding energies for the two N1s signals do not differ much for all fresh and used VZrPON catalysts; however, their relative intensity changes. In general, the percentage of NH_2 and NH surface species (peak at $E_B \approx 398$ eV) dominates in the fresh VZrPON catalysts, in particular for higher V/Zr ratios, while the percentage of NH_4^+ species (peak at $E_B \approx 400$ eV) increases after use in the ammoxidation reaction. Interestingly, the used oxide precursor VZrPO-0.1A after ammoxidation contains only NH_4^+ surface species, reflected by a single N1s peak at 399.8 eV.

3.2.4. FTIR results

More detailed information about structural changes upon treatment in NH_3 flow can be obtained by comparing the ATR spectra in Fig. 5. Bands between 1500 and 1200 cm^{-1} ν(P═O), 1200 and 900 cm^{-1} ν(P-O) and 650 and 300 cm^{-1} δ(O—P—O) are characteristic for oxidic phosphorus compounds [39].

The spectrum of sample VZrPO-0.1 shows a broad P—O band at 999 cm^{-1} (Fig. 5A). The V═O vibration is expected around 1030 cm^{-1} [40], yet the V content might be too low for this vibration being visible in the spectrum. Only in the spectra of VZrPO-0.5 and -0.9 with markedly higher V content the V═O vibration is superimposed on the P—O band, which shifts the maximum of the sum band to 1023 cm^{-1} and 1045 cm^{-1}, respectively. In the spectrum of VZrPO-0.5, additional bands appear below 1000 cm^{-1} which can be considered as a fingerprint of the crystalline $ZrV_{2-x}P_xO_7$ phase. In agreement with XRD data (Fig. 3A), they become more pronounced for VZrPO-0.9, in which this phase is dominating. Bands in this range arise from ν(M—O—M) vibrations [41]. Thus, P—O—P bridging groups in sodium pyrophosphate $Na_4[P_2O_7]$ give rise to the stretching vibrations ν_{as} = 915 cm^{-1} and ν_s = 730 cm^{-1}, while V—O—V units in sodium pyrovanadate $Na_4[V_2O_7]$ vibrate at ν_{as} = 710 cm^{-1} and ν_s = 533 cm^{-1} [42,43]. Based on these data, bands at 874 cm^{-1} and 650 cm^{-1} in Fig. 5 (top) are assigned to ν(P—O—P) and those at 715 cm^{-1} and 533 cm^{-1} to ν(V—O—V) vibrations. The band around 800 cm^{-1} which is particularly strong in sample VZrPO-0.9 containing the mixed $ZrV_{2-x}P_xO_7$ as main component may come from a V—O—P stretching mode. The very weak band around 1620 cm^{-1} arises from a $\delta(H_2O)$ vibration.

Treatment in NH_3 flow gives rise to a new band at around 1430 cm^{-1}, which is typical for NH_4^+ species (Fig. 5, bottom) [44]. Moreover, the bands assigned to the crystalline $ZrV_{2-x}P_xO_7$ phase disappear completely in sample VZrPON-0.5 and widely in sample VZrPON-0.9, in agreement with XRD and NMR data (Figs. 3B and 4). For VZrPON-0.9, new bands at 977, 887 and 817 cm^{-1} can be

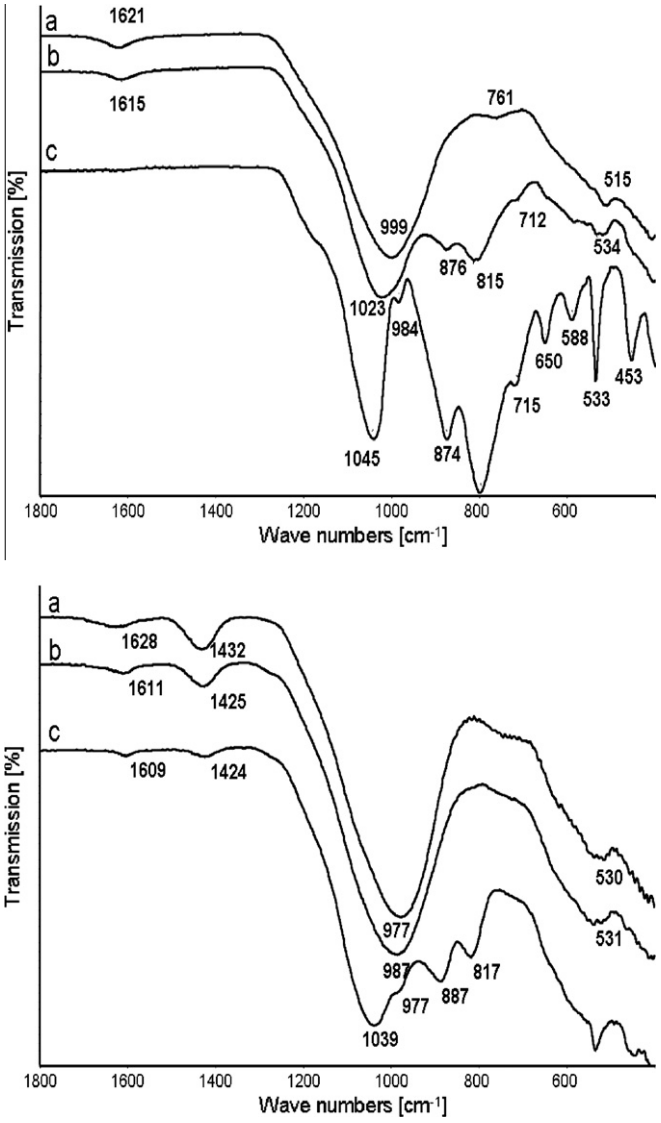

Fig. 5. ATR spectra of fresh VZrPO (top) and VZrPON (bottom) catalysts with different V/Zr ratios (*a* = 0.1, *b* = 0.5 and *c* = 0.9).

observed, which presumably hide those of the residual crystalline $ZrV_{2-x}P_xO_7$ phase. Obviously, the M—O—M sites (M = P and/or V) in this phase are split by ammonia treatment, which makes the sample widely amorphous (compare also Fig. 3B). Bands at 887 and 817 cm^{-1} may originate from condensed P–N units [45,46], while the shoulder at 977 cm^{-1} can be attributed to P—O(H) groups [45]. Possibly, P—O—M bonds (M=P or V) undergo ammonolysis according to Eq. (2), as likewise observed also for VPO catalysts [11].

$$P{-}O{-}M + NH_3 \rightarrow P{-}NH_2 + HO{-}M \quad (2)$$

The ATR spectra of all samples after use in the ammoxidation of 3-PIC are shown in Fig. 6. By comparing the spectra of the VZrPO oxide precursors before and after use (Figs. 5 and 6, top) it is clearly seen that position and shape of the bands do almost not change during treatment in ammoxidation feed flow. The only difference is a NH_4^+ band that arises in the spectra at lower V content, but is hardly seen in the used sample VZrPO-0.9. Interestingly, the $ZrV_{2-x}P_xO_7$ fingerprint is still well visible in the spectra of the used oxide precursors with V/Zr $\geqslant$ 0.5, indicating a high stability of this phase under ammoxidation conditions.

In the spectrum of used VZrPON-0.9 with the highest V content, the $ZrV_{2-x}P_xO_7$ fingerprint signals at 879, 808 and 719 cm^{-1} gain intensity after use in the reaction (compare Figs. 5c and 6c , bottom), suggesting that this phase is restored under ammoxidation conditions. Also bands of NH_4^+ at 1425 cm^{-1} appear again, but their intensities are almost equal and do not correlate with V concentration. Especially for used VZrPON-0.9, the intensity of this band is higher compared to the corresponding spectra before and after nitridation.

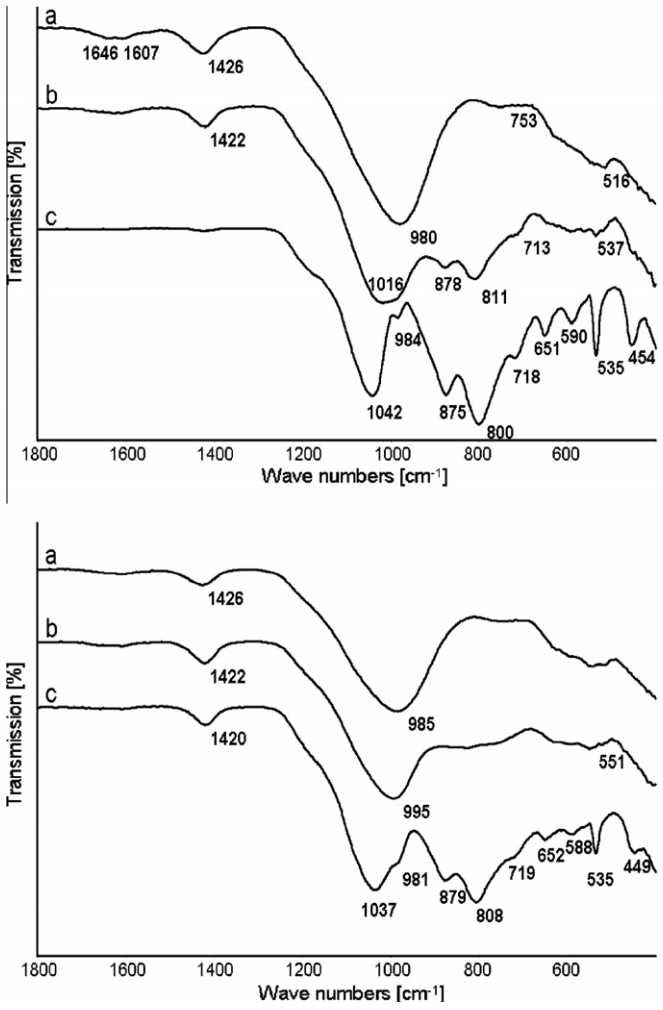

Fig. 6. ATR spectra of used VZrPO (top) and VZrPON (bottom) catalysts with different V/Zr ratios (*a* = 0.1, *b* = 0.5 and *c* = 0.9).

To support the identification of different nitrogen-containing sites in the VZrPON series, FTIR spectra of self-supporting wafers were recorded at 300 °C in vacuum (Fig. 7) from fresh VZrPON samples. For comparison, IR bands of phosphorodiamidic acid used as reference are presented in Table 3 [47]. On this basis, the band at 1558 cm^{-1} in Fig. 7 is assigned to P—NH_2 vibrations, while the band at 1420 cm^{-1} is typical for a $\delta(NH_4^+)$ vibration. This band has also been observed in the ATR spectra of fresh and used VZrPON samples recorded under ambient conditions (Figs. 5 and 6). Moreover, the presence of NH_4^+ surface species is confirmed by the XPS results (Table 2, N1s peak around 400 eV). No bridging P—NH—P unit can be identified, since bands around 3074 cm^{-1} (not shown in Fig. 7) are missing. Vibrations of doubly bound —P=N—P units formed by condensation of neighbouring P—NH_2 and M—OH groups (Eq. (3)) are expected in a range from 1420 to 1250 cm^{-1} (ν_{as}) and 950 to 800 cm^{-1} (ν_s) [42].

$$P{-}NH_2 + HO{-}M \rightarrow P{=}N{-}M + H_2O (M{=}P \text{ or } Zr) \quad (3)$$

A band at 1372 cm^{-1}, which could arise from ν_{as} (—P=N—P) vibrations, is well seen in the spectrum of sample VZrPON-0.9 (Fig. 7c). In agreement with XPS data, this suggests that N might be preferentially incorporated in the vicinity of phosphorus.

Brønsted surface sites have been analysed by adsorption of pyridine. Relative band areas at 1545 cm^{-1} are shown in Table 4 for the fresh and used oxide and oxynitride catalysts with V/Zr = 0.1. The corresponding spectra are plotted in Fig. S4 (Supporting information). These four catalysts were chosen, since the conversion $X_{3\text{-PIC}}$ is nearly identical for the oxide and oxynitride, but their selectivity $S_{3\text{-CP}}$ is different (Fig. 1). As proved by time-dependent catalytic tests (Fig. 2) and XPS results (Table 2), the structure of oxynitride and oxide catalysts changes during catalytic reaction. Therefore, besides the fresh samples, also the used oxide and oxynitride were investigated by pyridine adsorption to identify the number acid sites.

Unfortunately, the characteristic band for Lewis acid sites at 1445 cm^{-1} in the fresh oxynitride VZrPON-0.1 is partly superimposed by a second broad band, which may be assigned to NH_4^+ sites (see Fig. S4). For this reason, only the Brønsted band at 1545 cm^{-1} has been analysed for evaluating surface acidity. From Table 4, it is evident that the number of Brønsted acid sites slightly increased during the ammoxidation reaction for both oxide and oxynitride catalyst. In general, the oxynitride catalysts possess more Brønsted acidic sites than the corresponding oxide catalyst.

3.3. Structural changes during NH_3 treatment followed by in situ-EPR/UV–vis/Raman spectroscopy

While FTIR spectroscopy is sensitive to detect structural modifications, EPR and UV–vis spectroscopy are complementary methods to follow changes of the V valence state during nitridation, in addition to the chemical environment. The treatment of the VZrPO oxide precursors in a diluted 20% NH_3/N_2 stream has been investigated by simultaneous in situ-EPR/UV–vis/Raman spectroscopy. Samples were heated in N_2 flow at 120 °C for 90 min, followed by a treatment in NH_3/N_2 at a maximum temperature of 410 °C. EPR spectra recorded at elevated temperature are shown in Fig. S2 (Supporting information).

However, for deriving spin Hamiltonian parameters by spectra simulation, EPR spectra were measured at room temperature before any treatment as well as after treatment in N_2 and in NH_3/N_2 flow and cooling in the same atmosphere, since this led

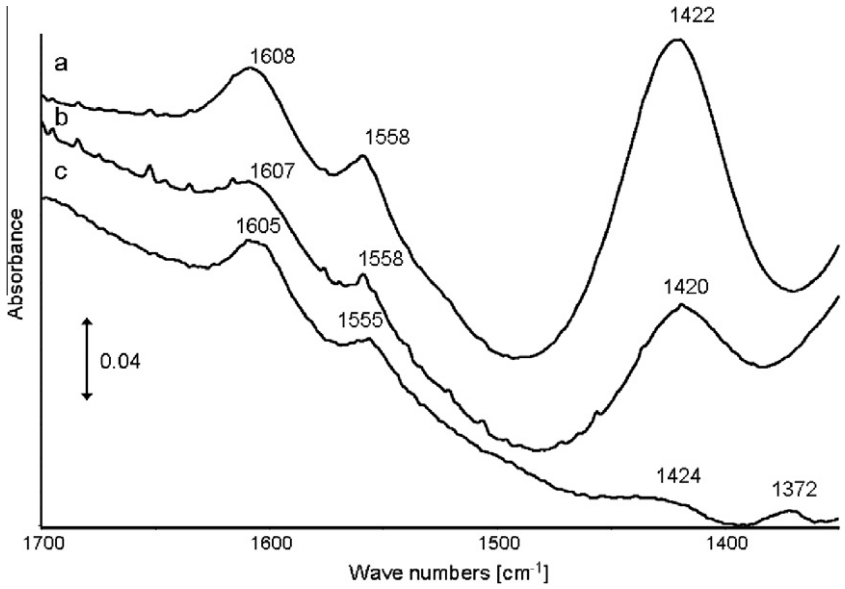

Fig. 7. FTIR spectra of fresh VZrPON catalysts with different V/Zr ratios (a = 0.1, b = 0.5 and c = 0.9) measured in transmission mode at 300 °C in vacuum.

Table 3
Nitrogen-containing species in $HPO_2(NH_2)_2$ and their vibration modes at 120 °C.

Wave number (cm^{-1})	Assignment
3074	ν_s (P)—NH—(P)
870 and 696	ν_{as}, ν_s P—NH—P
3385; 3269; 1586	ν_{as}, ν_s, δ(P)—NH_2
1467	δNH_4^+
830–750	ν_s P═N—
690	ν_s P—N(P)—P

Table 4
Relative concentration of Brønsted acid sites (a.u.) for the fresh and used oxide and oxynitride with V/Zr = 0.1, obtained by normalizing the area (integral) of the FTIR band of adsorbed pyridine at 1545 cm^{-1} on the BET surface area (A_B/S_{BET}).

Sample	A_B/S_{BET}·1000
VZrPO-0.1	8.9
VZrPON-0.1	16.8
VZrPO-0.1A	12.6
VZrPON-0.1A	27.8

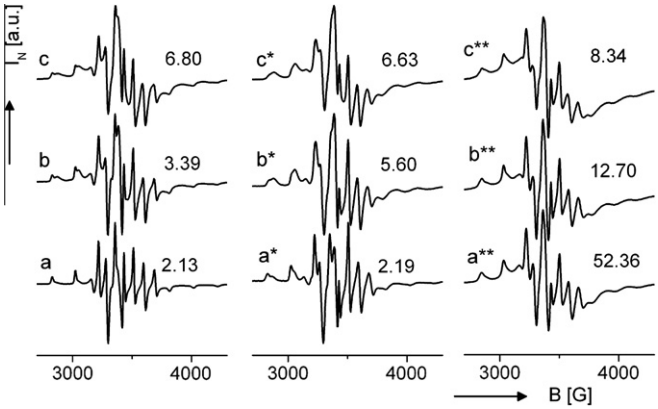

Fig. 8. Normalized in situ-EPR spectra of VZrPO precursors with different V/Zr ratio (a = 0.1, b = 0.5 and c = 0.9) measured at room temperature: a–c untreated oxide precursor; a^*–c^* after heating in N_2 flow for 90 min at 120 °C; a^{**}–c^{**} after heating in NH_3/N_2 flow for 30 min at 410 °C. The numbers on the right side of each spectrum denote the signal intensities I_{int} (double integrals).

to spectra with higher quality. In Fig. 8, normalized EPR spectra are presented to better visualize changes of the spectral shape. The true intensity is evident from the double integrals given on the right side of each EPR spectrum. It has to be mentioned that the only V species accessible by EPR spectroscopy under these conditions is V^{4+} in square-pyramidal or octahedral oxygen coordination, while tetrahedrally coordinated V^{4+} as well as V^{3+} are usually not visible at ambient and elevated temperature, due to short relaxation times and V^{5+} is not paramagnetic.

All spectra show a well-resolved hyperfine structure multiplet which arises from isolated VO^{2+} species in square-pyramidal or octahedral coordination due to the coupling of the electron spin of V^{4+} (S = ½) with the nuclear spin of vanadium (I = 7/2). Two single VO^{2+} sites (labelled S_1 and S_2) with slightly different spin Hamiltonian parameters and a broad isotropic singlet caused by cluster-like magnetically interacting VO^{2+} species (denoted as C) had to be superimposed to properly reproduce the experimental spectra (Table 5). As expected, the contribution of the cluster signal increases with rising V content within each series.

Spin Hamilton parameters for each isolated site S_1 and S_2 in sample VZrPO-0.1 before any treatment (spectrum a in Fig. 8) and for all VZrPO samples after heating in NH_3/N_2 flow (spectra a^{**}–c^{**} in Fig. 8) are listed in Table 5. A plot of the experimental together with the calculated spectra is shown in Fig. S3. The intensity ratio of the single and cluster site signals, S_1:C:S_2, is also shown. The parameter $\Delta g_{||}/\Delta g_{\perp}$ (with $\Delta g_{||} = g_{||} - g_e$ and $\Delta g_{\perp} = g_{\perp} - g_e$) is a measure for the overall distortion of an axial site. The larger $\Delta g_{||}/\Delta g_{\perp}$, the higher is the distortion, in other words, the shorter the V═O bond and the longer the V—O bonds in the basal plane of the VO^{2+} octahedron [48,49]. β_2^{*2} is the in-plane delocalization coefficient. It is a measure for the extent to which the unpaired electron of the V^{4+} is delocalized towards the four oxygen ligands within the basal plane of the VO^{2+} species, i.e., a measure of the degree of covalency of the V—O bonds. β_2^{*2} = 1 when the unpaired electron is completely localized at the V^{4+} nucleus [44]. β_2^{*2} can be calculated using Eq. (4) in which P = 184.5 G for the free V^{4+} ion [50].

Table 5
Spin Hamiltonian parameters ($A_{||}$, $A_{\perp}$, $g_{||}$, $g_{\perp}$), β_2^{*2}, $\Delta g_{||}/\Delta g_{\perp}$ and S_1:C:S_2 ratio for in situ formed VZrPON catalysts.

EPR spectrum	VZrPO-0.1 (*a*)		VZrPON-0.1 (*a***)		VZrPON-0.5 (*b***)		VZrPON-0.9 (*c***)	
Species	S_{1a}	S_{2a}	S_{1a**}	S_{2a**}	S_{1b**}	S_{2b**}	S_{1c**}	S_{2c**}
$A_{||}$ (G)	202.3	198.5	192.8	181.8	190.5	184.4	188.0	188.5
$A_{\perp}$ (G)	74.1	69.5	69.0	54.4	68.7	53.9	67.3	53.8
$g_{||}$	1.923	1.933	1.937	1.939	1.940	1.938	1.942	1.939
$g_{\perp}$	1.978	1.976	1.981	1.972	1.981	1.972	1.981	1.971
$\Delta g_{||}/\Delta g_{\perp}$	3.26	2.63	3.08	2.09	2.98	2.12	2.83	1.98
β_2^{*2}	0.89	0.89	0.85	0.87	0.83	0.89	0.82	0.91
S_1:C:S_2	1:3.7:1		1:5.1:0.8		1:11.6:0.7		1:18.9:0.6	

$$\beta_2^{*2} = 7/6\Delta g_{||} - 5/12\Delta g_{\perp} - 7/6[(A_{||} - A_{\perp})/P] \quad (4)$$

For the untreated oxide precursors, the double integral intensities increase with rising V content as expected (Fig. 8*a*–*c*). There is not much change after heating in N_2 flow. However, the signal intensity grows strongly after treatment in NH_3/N_2 flow, which goes along with an increase in the relative contribution of the cluster signal. Interestingly, the gain in total intensity upon switch from N_2 to NH_3/N_2 flow, which reflects the reduction in V^{5+} to V^{4+} is most pronounced for sample VZrPO-0.1 with the lowest V content, while it is almost negligible for VZrPO-0.9 (Fig. 8*a***–*c***). The reason is probably that with rising V content, the reduction in vanadium goes partially to EPR-silent V^{3+}. This is also supported by UV–vis data which will be discussed later.

Spin Hamiltonian parameters of isolated VO^{2+} provide information about the local environment of such species. The g and A parameters of species S_1 in VZrPON-0.1 after NH_3 treatment (Table 5) are very similar to those of partially reduced $VOPO_4{\cdot}2H_2O$ which contains single VO^{2+} defects ($g_{||} = 1.938$, $g_{\perp} = 1.982$, $A_{||} = 192$ G, $A_{\perp} = 69$ G [51,52]). In this structure, VO_5 chains are linked together by PO_4 tetrahedra resulting in polymeric $(VOPO_4)_n$ layers. The axial geometry of the second isolated VO^{2+} species S_2 in VZrPON-0.1 is less distorted, as can be concluded from the smaller $\Delta g_{||}/\Delta g_{\perp}$ ratio (Table 5). The spin Hamiltonian parameters of this site are similar to those derived for the corresponding phosphorus-free VZrON catalyst ($g_{||} = 1.940$, $g_{\perp} = 1.980$, $A_{||} = 182.4$ G, $A_{\perp} = 61.9$ G, Fig. S5). Thus, species S_2 can be attributed to isolated VO^{2+} sites connected via oxygen bridges to Zr rather than to P. From Table 5, it is evident that the two isolated species S_1 and S_2 are equally abundant in the untreated sample VZrPO-0.1, while the intensity of species S_2 decreases in relation to that of species S_1 in VZrPON-0.1 after NH_3 treatment. This suggests that VO^{2+} species connected to Zr (S_2) are easier reduced to EPR-silent V^{3+} than those connected to P (S_1).

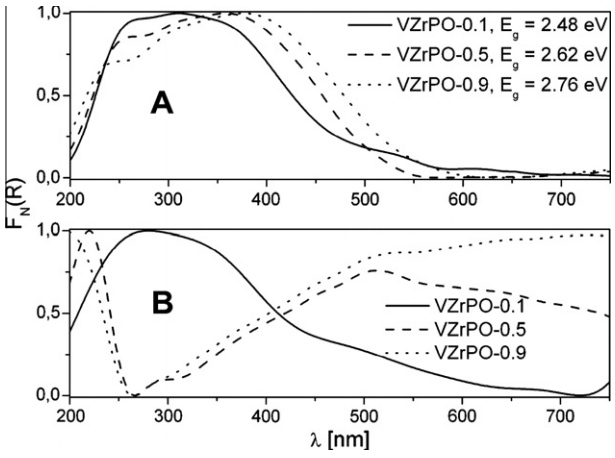

Fig. 9. Normalized in situ-UV–vis spectra measured at room temperature for VZrPO oxide precursors with different V/Zr ratios after heating in N_2 flow for 90 min at 120 °C (A) and after heating in NH_3/N_2 flow for 30 min at 410 °C (B). E_g denotes the absorption edge energy.

With rising V content, $A_{||}$ values of sites S_1 and S_2 become more similar, converging at ca. 188 G in sample VZrPON-0.9 (Table 5). This sample contains Zr, P and V in almost equal amounts. Given that a rather homogeneous distribution of V is established throughout the structure, this would imply that both V sites S_1 and S_2 should be connected via oxygen bridges to both P and Zr, which may average to some extent the differences in their local environment.

When β_2^{*2} and $\Delta g_{||}/\Delta g_{\perp}$ values for VZrPON samples in Table 5 are compared to those of previously described VAlON catalysts ($\beta_2^{*2} = 0.69$ – 0.67 and $\Delta g_p/\Delta g_s = 3.46$–$3.30$ [13]), in which V—N bonds are present, marked differences are evident. This suggests that a partial substitution of V—O by V—N moieties observed for VAlON can be excluded for VZrPON catalysts. In other words, the coordination sphere of V sites in the latter catalysts is most probably almost N-free and this agrees properly with the results of XPS and FTIR spectroscopy which also suggest that N might be preferentially linked to P and not to V.

UV–vis spectra after treatment in N_2 flow recorded along with the EPR spectra are shown in Fig. 9 A. They are characterized by a broad band at lower wavelength which arises from charge-transfer (CT) transitions of pentavalent V^{5+} [53]. The absorption edge energy E_g for this transition was determined by finding the intercept of the straight line in the low-energy rise of a plot of $[F(R)h\nu]^2$ against $h\nu$, where $h\nu$ is the incident photon energy [54].

The absorption edge energy E_g increases with rising V content. As expected, this points to increasing formation of vanadyl clusters, which is also evident from the broad background signal in the EPR spectra for VO^{2+} species. Upon heating in an NH_3/N_2 flow, the intensity of the CT bands below 400 nm decreases while it rises strongly in the visible range above 500 nm, where d–d transitions of reduced V^{4+} and V^{3+} species occur (Fig. 9B) [55]. It is clearly seen that the increase in absorbance is highest for sample VZrPON-0.9 with the highest V content, suggesting strongest reduction. Most probably, this leads, besides EPR-visible V^{4+}, to a certain percentage of EPR-silent V^{3+}, which accounts for the intensity loss of the EPR signal of sample VZrPON-0.9 (Fig. 8c**), while d–d bands of V^{4+} and V^{3+} superimpose in the high-wavelength range of the UV–vis spectra and cannot be distinguished from each other (Fig. 9B).

In situ Raman spectra recorded along with EPR and UV–vis spectra are plotted in Fig. 10 only for sample VZrPO-0.9 with the highest V content before and after treatment in NH_3/N_2 flow, since for the other catalysts with lower V/Zr ratio the signal-to-noise ratio was too low. Bands at 994, 702, 525,486, 405 and 285 cm^{-1} are assigned to V_2O_5 nanocrystals [56], which are obviously too small to be detected in the XRD pattern of Fig. 3A. This is in agreement with results of ^{51}V MAS NMR (see Fig. 4). Bands at 883 and 817 cm^{-1} may be assigned to vibrations of V—O—P units, while the one at 1045 cm^{-1} might arise from the V=O vibration of single

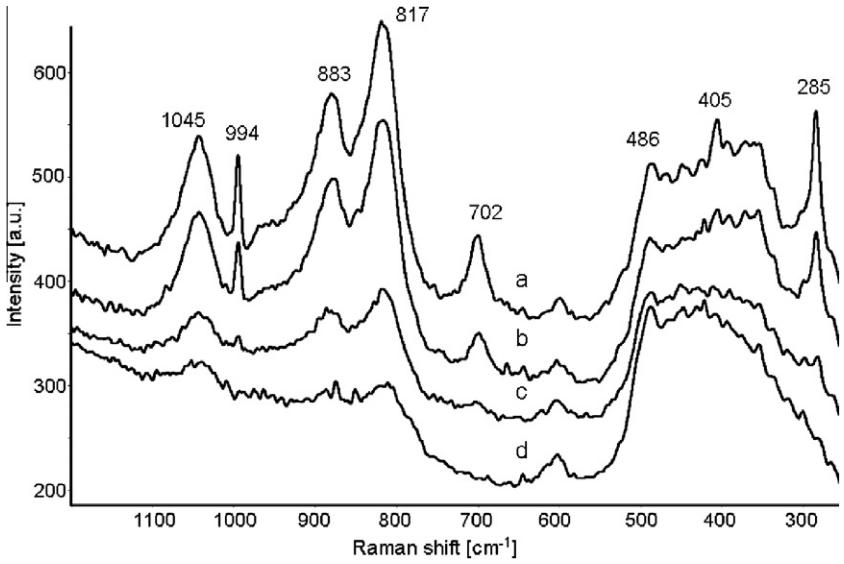

Fig. 10. In situ Raman spectra of sample VZrPO-0.9 measured at room temperature after heating in N_2 flow for 90 min at 120 °C (a) and after heating in NH_3/N_2 flow for 30 min at 110 °C (b), for 90 min at 160 °C (c) and for 30 min 300 °C (d).

V^{5+} sites [57,58]. Most probably, these bands belong to the crystalline $ZrV_{2-x}P_xO_7$ phase. It can be seen that during NH_3 treatment, the intensity of all bands decreases. This is due to the reduction in V^{5+}. However, it is also evident that the bands of V_2O_5 nanocrystals decrease faster than those of the $ZrV_{2-x}P_xO_7$, suggesting that the latter is more stable against reduction by NH_3.

3.4. Structure–reactivity relationships in VZrPON catalysts

In comparison with the best previously tested P-free VZrON catalyst, the highest achievable conversion of 3-PIC obtained over VZrPON catalysts is only about half as high, while the 3-CP selectivity over VZrPON-0.9 exceeds that of the best P-free VZrON-0.25 catalysts only slightly (Fig. 1). Marked structural changes caused by the incorporation of phosphorus might be responsible for this different catalytic behaviour. This is evidenced by a variety of characterization methods. For VZrON catalysts, pronounced formation of crystalline ZrO_2, though containing some dispersed V sites in Zr lattice positions, forces agglomeration of the majority of V within V_xO_y clusters in which vanadium takes markedly higher mean valence states (between 4.3 and 4.9 [13]) in comparison with the VZrPON catalysts in this work. Moreover, the surface of the P-free VZrON catalysts remained essentially free of N, since the latter was almost completely enriched in the bulk structure.

The incorporation of P leads first of all to a higher dispersion of vanadium in the VZrPON catalysts. This is clearly shown by the VO^{2+} EPR spectra which possess resolved hyperfine structure (Fig. 8). Moreover, the formation of a crystalline mixed $ZrV_{2-x}P_xO_7$ phase suppresses the agglomeration of VO_x species. This phase, in which V is tetrahedrally coordinated by oxygen, was confirmed by XRD (Fig. 3, Fig. S1), NMR (Fig. 4) and ATR (Figs. 5 and 6). Both effects, high V site isolation and low oxygen coordination, are known to diminish catalytic activity but improve selectivity in selective oxidation reactions [59,60]. As far as the mean V valence state is considered, it turned out that a V valence close to +4 might be optimal [13]. A high percentage of V^{5+} increases activity (though at the expense of selectivity), while deep reduction to V^{3+} deactivates the catalyst. Coupled in situ-EPR/UV–vis results suggest that in the VZrPON-0.9 catalyst with the highest V content, a marked reduction to inactive V^{3+} takes place during treatment in NH_3/N_2 flow, which might account for the drop in activity (see Figs. 8 and 9).

Surprisingly, $S_{3\text{-CP}}$ values are not much higher than for P-free VZrON catalysts at low V content (see Fig. 1). This suggests that factors other than V dispersion might govern the 3-CP selectivity. For VZrON and VAlON oxynitrides, the close vicinity of V and N sites within V—N—M moieties (M=Al or Zr) as well as negligible surface acidity was found to be beneficial for high catalytic performance, besides high V dispersion [13]. While V sites are highly dispersed also in VZrPON catalysts, XPS, FTIR and EPR results suggest that nitrogen in these catalysts, although being present on the surface (in contrast to VZrON [13]), is preferentially linked to P but not incorporated in the vicinity of vanadium. This possibly disfavours a concerted oxidation/N-insertion mechanism catalysed by —O—V—N—M—O— sites, which could lower the 3-CP selectivity.

From Table 1, it is evident that initially N-free VZrPO precursors take up nitrogen when exposed to ammoxidation conditions, while the corresponding VZrPON catalysts loose nitrogen under the same conditions. A similar behaviour has been observed by Florea et al. for VAlO and VAlON catalysts in the ammoxidation of propane [57,61]. In their experiments, the equilibrium N content established during reaction was governed by the NH_3/O_2 ratio in the feed. Moreover, it was found that the selectivity of acrylonitrile increased with the total N content in the catalysts, while the propane conversion was not influenced [61]. In the series of our used VZrPON catalysts, a similar dependence of the 3-CP selectivity is found, yet not on the total N content but on the surface N content reflected by the XPS N/P ratio (compare Fig. 1 and Table 1), which is more relevant for the catalytic behaviour. This is not only evident within the series of VZrPON catalysts, but also from a comparison of $S_{3\text{-CP}}$ and the N/P ratio of the used VZrPO catalyst in which N originates exclusively from the reactant feed. This suggests that the same surface N species are formed in VZrPO as well as in VZrPON catalysts under reaction conditions, as supposed accordingly by Florea et al. for the VAlO/VAlON system.

Besides the surface N content, it was supposed that the surface acidity may influence the 3-CP selectivity as well, since the incorporation of P in the surface of VZrPON catalysts might lead to some Brønsted acidity by formation of P—OH bonds and to Lewis acidity arising from empty 3d orbitals of P, in contrast to VZrON being free of such sites [13]. Acidic surface sites can hinder fast desorption of the basic nitrile product molecules and, thus, diminish selectivity as a consequence of deep oxidation. As mentioned previously,

NH_3-TPD cannot be used for acidity determination in these systems and from FTIR spectroscopy of adsorbed pyridine, the characteristic band of pyridine adsorbed on Lewis sites is not accessible, since the relevant wave number range is masked by an NH_4^+ band. However, a band being characteristic of Brønsted sites is clearly seen in both VZrPO and VZrPON catalysts (Fig. S4), which was essentially missing in the respective P-free catalysts [9]. Nevertheless, the selectivity of P-free, non-acidic VZrON is lower compared to VZrPON (Fig. 1). This suggests that a certain amount of surface N species, which are present on VZrPON (Table 1) but completely missing on P-free VZrON [13], might have a higher impact on 3-CP selectivity than surface acidity. It could be the reason why the N-containing surface of VZrPON catalysts, despite its higher surface acidity (Table 4), is more selective than the completely N-free though non-acidic surface of VZrON. The dominating impact of surface N species is also evident by comparing the selectivity of VZrPO-0.1 and VZrPON-0.1 (Fig. 1). The surface concentration of Brønsted sites is higher on the latter catalyst (Table 4). Nevertheless, this catalyst is more selective (Fig. 1) and this is most probably due to its higher N/P surface ratio (Table 1). The selectivity-improving impact of nitrogen is also supported by catalytic tests with varying air/NH_3 flow ratio, in which highest selectivities were found for lowest $F(\text{air})/F(NH_3)$ ratios (Fig. 2B).

4. Conclusions

In comparison with previously tested phosphorus-free VZrON oxynitrides [13], the incorporation of P in VZrPON catalysts leads to lower activities, while the 3-CP selectivity is only slightly improved when the V/Zr ratio approaches unity. With rising V content, a crystalline mixed $ZrV_{2-x}P_xO_7$ phase is formed in the VZrPO oxide precursors, which includes a marked percentage of the total vanadium in the form of single $V^{5+}O_4$ sites. Upon nitridation in NH_3 flow, this phase is degraded and V^{5+} is to a considerable extent reduced to V^{4+} or even to V^{3+} when V/Zr = 0.9. High V dispersion and marked reduction are considered as main reasons for lower activity in comparison with the P-free VZrON catalysts. During treatment in NH_3 flow, N is preferentially incorporated in the vicinity of P, leading to P-NH_2 and P═N—M (M = P, Zr) groups, while the formation of —V—N—M— moieties, considered to be essential for effective ammoxidation following a concerted oxidation/N-insertion mechanism, is suppressed. The selectivity of 3-CP increases with the amount of N species on the catalyst surface. The impact of these N species on 3-CP selectivity is more dominant in comparison with surface acidity introduced by the incorporation of P. This could explain why VZrON catalysts, in which N is enriched in the bulk leaving the catalyst surface widely N-free, are less selective than VZrPON catalysts that do contain surface N species, although the latter show a higher surface acidity which could favour strong surface adsorption followed by deep oxidation of the 3-CP product molecules. In summary, it must be concluded that the incorporation of phosphorus into VZrPON oxynitrides does not improve their catalytic performance in comparison with their P-free VZrON counterparts.

Acknowledgment

We thank C. Domke and R. Pérez Vélez for measuring the FTIR and ATR spectra. We appreciate the experimental support of F. Emmerling and M. Klimakow at BESSY. Financial support by Deutsche Forschungsgemeinschaft (grant No. BR 1380/15-1) and Max-Buchner-Forschungsstiftung (grant of C. Janke) is gratefully acknowledged.

Appendix A. Supplementary material

Supplementary data associated with this article can be found, in the online version, at doi:10.1016/j.jcat.2010.11.008.

References

[1] K.-K. Moll, E. Fischer, Chem. Technol. 20 (1968) 600 (Leipzig).
[2] M.C. Sze, A.P. Gelbein, J.E. Paustian, DE 2435134C2, The Lummus Co., 1975.
[3] M.C. Sze, A.P. Gelbein, J.E. Paustian, DE 2435134A1, The Lummus Co., 1974.
[4] R. Chuck, Appl. Catal. A: Gen. 280 (2005) 75.
[5] P. Cavalli, F. Cavani, I. Manenti, F. Trifiro, Catal. Today 1 (1987) 245.
[6] W.S. Chen, H.B. Chiany, M.D. Lee, J. Chin. Chem. Eng. 25 (1994) 45.
[7] A. Andersson, S.L.T. Andersson, G. Centi, R.K. Grasselli, M. Sanati, M. Trifiro, Appl. Catal. A 113 (1994) 43.
[8] L.v. Hippel, A. Neher, D. Arntz, EP 0726092 B1, Degussa-Hüls AG, 1999.
[9] V.N. Kalevaru, B. Lücke, A. Martin, Stud. Surf. Sci. Catal. 175 (2010) 393.
[10] V.N. Kalevaru, B.D. Raju, V.V. Rao, A. Martin, Appl. Catal. A: Gen. 352 (2009) 223.
[11] G.Y. Xie, H. Chi, Ind. J. Chem. Technol. 14 (2007) 371.
[12] K.V.R. Chary, C.P. Kumar, K.R. Reddy, T. Bhaskar, T. Rajiah, Catal. Commun. 3 (2002) 7.
[13] C. Janke, J. Radnik, U. Bentrup, A. Martin, A. Brückner, ChemCatChem 1 (2009) 485.
[14] A. Andersson, S.T. Lundin, J. Catal. 58 (1979) 383.
[15] B. Lücke, K.V. Narayana, A. Martin, K. Jähnisch, Adv. Synth. Catal. 346 (2004) 1407–1424.
[16] M. Sanati, A. Andersson, J. Mol. Catal. 59 (1990) 233.
[17] Y. Zhang, A. Martin, H. Berndt, B. Lücke, M. Meisel, J. Mol. Catal. A 110 (1997) 919.
[18] A. Brückner, Catal. Rev. Sci. Eng. 45 (2003) 97.
[19] P. Mars, D.W. van Krevelen, Chem. Eng. Sci. 3 (1954) 41.
[20] A. Baiker, P. Zollinger, Appl. Catal. 10 (1984) 231.
[21] A. Andersson, J. Catal. 100 (1986) 414.
[22] R. Prasad, A.K. Kar, Ind. Eng. Chem. Process Des. Dev. 15 (1976) 170.
[23] G. Busca, F. Cavani, F. Trifiro, J. Catal. 106 (1987) 471.
[24] A. Martin, A. Brückner, Y. Zhang, B. Lücke, in: H.U. Blaser, A. Baiker, R. Prins (Eds.), Heterogeneous Catalysis and Fine Chemicals IV, Elsevier Science B.V, Amsterdam, 1997, p. 377.
[25] A. Brückner, A. Martin, B. Kubias, B. Lücke, J. Chem. Soc. Faraday Trans. 94 (1998) 2221.
[26] R. Prada Silvy, M. Florea, N. Blangenois, P. Grange, AIChE J 49 (2003) 2228.
[27] M. Olea, M. Florea, I. Sack, R. Prada Silvy, E.M. Gaigneaux, G.B. Marin, P. Grange, J. Catal. 232 (2005) 152.
[28] N. Fripiat, M.-A. Centeno, P. Grange, Chem. Mater. 11 (1999) 1434.
[29] A. Brückner, Chem. Commun. 13 (2005) 1761.
[30] G.P. Lozos, B.M. Hofman, C.G. Franz, Quantum Chemistry Program Exchange, 1973, p. 265.
[31] Powder Diffraction File (PDF-2 Release 2004) database of the International Centre of Diffraction Data (ICDD), PDF No. [88-587].
[32] Powder Diffraction File (PDF-2 Release 2004) database of the International Centre of Diffraction Data (ICDD), PDF No. [86-781].
[33] C. Hudalla, H. Eckert, R. Dupree, J. Phys. Chem. 100 (1996) 15986.
[34] V. Korthuis, N. Khosrovani, A.W. Sleight, Chem. Mater. 7 (1995) 412.
[35] A.A. Shubin, O.B. Lapina, E. Bosch, J. Spengler, H. Knözinger, J. Phys. Chem. B 103 (1999) 3138.
[36] W.E. Morgan, J.R. Van Wazer, W.J. Sec, J. Am. Chem. Soc. 95 (3) (1973) 751.
[37] J. Mendialdua, R. Casanova, Y. Barbaux, J. Electron Spectroc. Relat. Phenom., 71 (1995) 249.
[38] H. Wiame, L. Bois, P. Lharidon, Y. Laurent, P. Grange, vol. 101–103, 1997, p. 755.
[39] K. Nakamoto, Infrared and Raman Spectra of Inorganic and Coordination Compounds, Part A, John Wiley & Sons, Inc., 1997. p. 266.
[40] L.J. Burcham, G. Deo, X. Gao, I.E. Wachs, vol. 11/12, 2000, p. 85.
[41] K. Nakamoto, Infrared and Raman Spectra of Inorganic and Coordination Compounds, Part A, John Wiley & Sons, Inc., 1997. pp. 236–237.
[42] W. Bues, K. Buchler, P. Kuhnle, Z. Anorg. Chem. 8 (1963) 325.
[43] R.G. Brown, S.D. Ross, Spectrochim. Acta 28 (1972) 1263.
[44] H. Siebert, Anwendung der Schwingungsspektroskopie in der Anorganischen Chemie, Springer-Verlag, Berlin, 1966.
[45] J.M. Devynck, E. Puskaric, R. de Jaeger, H. Heubel, J. Chem. Res. 5 (1977) 188.
[46] J. Weidlein, U. Müller, K. Dehnicke, Schwingungsfrequenzen I, Georg Thieme Verlag Stuttgart, New York, 1981.
[47] Y. Parent, L. Montagne, G. Palavit, J. Mater. Sci. 31 (1996) 3583.
[48] K. Nowinska, A.B. Wieckowski, Z. Phys. Chem. NF 162 (1989) 231.
[49] E.G. Derouane, A.J. Simoens, J.C. Védrine, Chem. Phys. Lett. 52 (1977) 549.
[50] L.J. Boucher, E.C. Tynan, T.F. Yen, Electron Spin Resonance of Metal Complexes, Plenum Press, New York, 1969.
[51] D. Ballutaud, E. Bordes, P. Courtine, Mater. Res. Bull. 17 (1982) 519.
[52] C. R' Kha, M.T. Vandenborre, J. Livage, J. Solid State Chem. 63 (1986) 202.
[53] M. Schraml-Marth, A. Wokaun, M. Pohl, H.-L. Krauss, J. Chem. Soc. Faraday Trans. 87 (1991) 2635.
[54] X. Gao, I.E. Wachs, J. Phys. Chem. B 104 (2000) 1261.

[55] A.B.P. Lever, Inorganic Electronic Spectroscopy, Elsevier Pub. Co., Amsterdam, 1968.
[56] M. Gotić, S. Popović, M. Ivanda, S. Musić, Mater. Lett. 57 (2003) 3186.
[57] M. Florea, R.P. Silvy, P. Grange, Appl. Catal. A: Gen. 286 (2005) 1.
[58] J.T. Kloprogge, R.L. Frost, Spectrochim. Acta 55 (1999) 163.
[59] T. Blasco, J.M. López-Nieto, Appl. Catal. 157 (1997) 117.
[60] P. Rybarczyk, H. Berndt, J. Radnik, M.-M. Pohl, O. Buyevskaya, M. Baerns, A. Brückner, J. Catal. 202 (2001) 45.
[61] M. Florea, R. Prada Silvy, P. Grange, Appl. Catal. A: Gen. 255 (2003) 289.